Theor. Comput. Fluid Dyn. (2008) 22: 65–82
DOI 10.1007/s00162-007-0066-x

ORIGINAL ARTICLE

Sébastien Barré · Christophe Bogey · Christophe Bailly

Direct simulation of isolated elliptic vortices and of their radiated noise

Received: 28 August 2006 / Accepted: 14 August 2007 / Published online: 2 October 2007

Abstract The aerodynamic evolution and the acoustic radiation of elliptic vortices with various aspect ratios and moderate Mach numbers are investigated by solving numerically the full compressible Navier–Stokes equations. Three behaviours are observed according to the aspect ratio $\sigma = a/b$ where a and b are the major and minor semi-axes of the vortices. At the small aspect ratio $\sigma = 1.2$, the vortex rotates at a constant angular velocity and radiates like a rotating quadrupole. At the moderate aspect ratio $\sigma = 5$, the vortex is initially unstable. However the growth of instability waves is inhibited by the return to axisymmetry which decreases its aspect ratio. The noise level becomes lower with time and the radiation frequency increases. For vortices with larger aspect ratios $\sigma \geq 6$, the return to axisymmetry does not occur quickly enough to stop the growth of instabilities, which splits the vortices. Various mergers are then found to occur. For instance in the case $\sigma = 6$, several successive switches between an elliptic state and a configuration of two co-rotating vortices are observed. The present results show that the initial value of the aspect ratio yields the relative weight between the return to axisymmetry which stabilizes the vortex and the growth of instabilities which tends to split it. Moreover the noise generated by the vortices is also calculated using the analytical solution derived by Howe (J. Fluid Mech. 71:625–673, 1975) and is compared with the reference solution provided by the direct computation. This solution is found to be valid for $\sigma = 1.2$. An extended solution is proposed for higher aspect ratios. Finally, the pressure field appears weakly affected by the switches between the two unstable configurations in the case $\sigma = 6$, which underlines the difficulty to detect the split or the merger of vortices from the radiated pressure. This study also shows that elliptic vortices can be used as a basic configuration of aerodynamic noise generation.

Keywords Kirchhoff's vortex · Vortex sound · Aeroacoustics · Direct numerical simulation

PACS 47.27.Sd · 47.27.ek · 47.32.cb

Communicated by M.Y. Hussaini.

S. Barré · C. Bogey · C. Bailly (✉)
Laboratoire de Mécanique des Fluides et d'Acoustique, UMR CNRS 5509, Ecole Centrale de Lyon,
36 avenue Guy de Collongue, 69134 Ecully Cedex, France
E-mail: christophe.bailly@ec-lyon.fr
E-mail: christophe.bogey@ec-lyon.fr

Present Address:
S. Barré
Dassault-Aviation, Aircraft and Stores Engineering Technical Directorate, 78 Quai Marcel Dassault, Cedex 300,
92552 St Cloud Cedex, France
E-mail: sebastien.barre@dassault-aviation.com

1 Introduction

Two-dimensional flows such as simple vortices have been intensively investigated in the past. These configurations seem elementary, but they are very useful to understand the evolution of coherent structures in numerous flows. For instance, elliptic vortices allow one to consider vortical configurations encountered in geophysical flows [19,20] or to model anisotropic effects of vortices [11,15].

The first works on elliptic vorticity distributions were analytical investigations of Kirchhoff's vortex, defined as an elliptical two-dimensional patch of uniform vorticity surrounding by irrotational fluid. Kirchhoff's vortex can be interpreted as a perpendicular section of an infinitely rectilinear vortex tube. This top hat vortex rotates about the center of the ellipse at a constant angular velocity Ω without change of shape [14]. The linear stability for aspect ratios $\sigma = a/b < 3$ was proven by Love [16], a and b being the major and minor semi-axes of the ellipse. More recently, Wan [23] and Dritschel [8] have shown theoretically and numerically that this vortex is nonlinearly stable only in the range of the linear stability $\sigma < 3$. Note also that the stability of the vortex has recently been linked to the spatial distribution of the strain rate, which must be of lower amplitude inside the vortex than just outside to ensure the stability, by Vosbeek et al. [22]. If $\sigma > 3$ the vortex is unstable, and the growth of instabilities can dramatically alter the shape of the vortex and can split it into two or more co-rotating vortices. The conditions for which the split generates two vortices have been investigated from energetic considerations by Dritschel [7,8]. In particular, this case is preferentially observed for an aspect ratio close to six. The time evolution can be also affected by the return to axisymmetry, namely the relaxation of the elliptic vortex towards a circular shape. Melander et al. [17] have shown that a vortex with smooth boundaries progressively sheds some vorticity with the formation of filaments, leading to a circular vortex. This phenomenon has been studied for stable elliptical vortices and has also been observed for co-rotating vortices [18]. However the circular state appears not to be obtained for vortices with sufficiently steep edge gradients [10].

The growth of instabilities and the return to axisymmetry occur in the case of an unstable Kirchhoff vortex. Instabilities may grow, and tend to split the vortex. At the same time, the return to axisymmetry takes place when a stagnation saddle point lies within the vortex and can affect the growth of these instabilities. Therefore, the evolution of the vortex depends on the process which will dominate the other one, and the dominant process is usually determined during the first few revolutions. The vortex development during this step can indeed change the relative weight of the two processes. Viscosity can also have some effects, as pointed out by Melander et al. [17], especially when splitting and merging occurs.

The first objective of this paper is to study the competition between the return to axisymmetry and the nonlinear evolution of instabilities, the effects of each process on the time evolution of the vortex, and the range of σ in which each phenomenon dominates the other one. This work also complements and extends the results obtained by previous numerical works mainly based on contour dynamics methods [7–10,22] or spectral methods [17,18] for inviscid incompressible flows, see for instance the introduction of Dritschel [9] and references herein. In the present simulations, the full 2D compressible Navier–Stokes are indeed solved for configurations at moderate Mach numbers.

In the present paper, the behaviours of Kirchhoff's vortices with initial aspect ratios $\sigma = 1.2, 5, 6, 12.5$ and 25 are calculated. In the first case $\sigma = 1.2$, the elliptic vortex is stable and very similar to a circular vortex. For $\sigma = 5$, the return to axisymmetry is expected to occur. For $\sigma \geq 6$ the vortex is strongly unstable and the growth of instabilities may have a notable effect on the vortex evolution. The full compressible Navier–Stokes equations are solved using high-order numerical schemes [1] developed for the direct computation of aerodynamic noise [2,4,12]. Both the flow field and the acoustic radiation of the elliptic vortices are thus obtained directly. This approach was for instance used to investigate the noise generated by two circular co-rotating vortices [3,5].

This work also offers new applications of classical results in aeroacoustics since viscosity and compressibility effects are taken into account. The Kirchhoff's elliptic vortex, in the same way as the case of two co-rotative vortices, is an interesting configuration since noise is generated by the vortex itself without interaction with solid boundary and without truncation of the source volume when an acoustic analogy is applied. The noise generated by vortices with aspect ratios $1.2 \leq \sigma \leq 6$ is presented with the aim of showing the influence of the initial aspect ratio on the acoustic radiation and the effects of the return to axisymmetry and merger processes on the pressure field. An analytical solution of the acoustic far-field derived by Howe [13] from the Lighthill's theory will be used to validate the computational results. This solution was, however, developed for small aspect ratios, and its validity for the present computed vortices will have to be investigated. The use of the Lighthill's theory will also provide an explicit relation between the characteristics of the vortex and the

radiated noise, and will make appear some key parameters of the sound generation. The study of the links between the dynamics of the elliptic vortices and the generated noise will give basic information regarding the description of the low-frequency noise radiated by large and persistent vortices, such as those produced in the wake of an aircraft at takeoff for instance.

The paper is organized as follows. Section 2 describes the numerical algorithm and the initial conditions used, whose expressions are detailed in Appendix A. The case of an aspect ratio close to unity, $\sigma = 1.2$, is investigated in Sect. 3. Then, the case of the moderate aspect ratio $\sigma = 5$ is studied in Sect. 4. The acoustic results are connected to the aerodynamic field and are also compared to the analytical solution [13] and presented in the Appendix B. Finally, Sect. 5 is devoted to three configurations with large aspect ratios $\sigma = 6$, 12.5 and 25. In particular, successive switches between an elliptic vortex and a configurations of two vortices are shown in the case $\sigma = 6$.

2 Numerical method

2.1 Governing equations

The two-dimensional compressible Navier–Stokes equations are solved in the conservative form

$$\frac{\partial \mathbf{U}}{\partial t} + \frac{\partial \mathbf{E}_e}{\partial x_1} + \frac{\partial \mathbf{F}_e}{\partial x_2} - \frac{\partial \mathbf{E}_v}{\partial x_1} - \frac{\partial \mathbf{F}_v}{\partial x_2} = 0$$

where $\mathbf{U} = (\rho, \rho u_1, \rho u_2, \rho e_t)^t$ is the unknown vector. The variables ρ, u_1, u_2 and e_t are, respectively, the density, the two velocity components and the total specific energy. The subscripts e and v denote the Euler and the viscous fluxes. For a perfect gas

$$\rho e_t = \frac{p}{\gamma - 1} + \frac{1}{2}\rho \left(u_1^2 + u_2^2\right)$$

where γ is the specific heat ratio and p the pressure. The Euler fluxes are given by

$$\mathbf{E}_e = \begin{pmatrix} \rho u_1 \\ \rho u_1^2 + p \\ \rho u_1 u_2 \\ (\rho e_t + p) u_1 \end{pmatrix} \qquad \mathbf{F}_e = \begin{pmatrix} \rho u_2 \\ \rho u_1 u_2 \\ \rho u_2^2 + p \\ (\rho e_t + p) u_2 \end{pmatrix}$$

and viscous fluxes by $\mathbf{E}_v = (0, \mathcal{T}_{11}, \mathcal{T}_{12}, u_i \mathcal{T}_{1i})^t$ and $\mathbf{F}_v = (0, \mathcal{T}_{21}, \mathcal{T}_{22}, u_i \mathcal{T}_{2i})^t$. The viscous stress tensor is defined by $\mathcal{T}_{ij} = 2\mu S_{ij}$ where μ is the dynamic molecular viscosity and S_{ij} the deviatoric part of the deformation stress tensor

$$S_{ij} = \frac{1}{2}\left(\frac{\partial u_i}{\partial x_j} + \frac{\partial u_j}{\partial x_i} - \frac{2}{3}\delta_{ij}\frac{\partial u_k}{\partial x_k}\right)$$

2.2 Numerical algorithm

Numerical schemes with low-dispersion and low-dissipation properties [1] are used. The spatial discretization is performed by an eleven-point stencil finite-difference scheme optimized in the wave-number space ensuring accuracy up to four points per wavelength. An optimized explicit six-stage Runge–Kutta algorithm is applied for time integration. To ensure stability, grid-to-grid oscillations are removed thanks to an eleven-point stencil selective filter without affecting the resolved scales, since only the short waves discretized by fewer than four points per wavelength are damped. Note that in the present work, direct numerical simulations of the Navier–Stokes equations are performed, without turbulence modelling. Moreover, the two-dimensional non-reflecting boundary conditions [21] are implemented. They are derived from the asymptotic solution of Euler's equations in the acoustic far-field, and thus allow to minimize acoustic reflections. This point is crucial for the direct calculation of the acoustic field.

Table 1 Parameters of the vortex for the different simulations: Reynolds number $Re_\Gamma = \Gamma/\nu$, where Γ is the circulation and ν is the kinematic viscosity; Mach number $M_e = U_e/c_0$ where $U_e = a\Omega$ is the velocity corresponding to the solid rotation of the vortex at the edge of the major semi-axis a and c_0 is the speed of sound

σ	ε	Re_Γ	M_e
1.2	0.09	6.2×10^5	0.29
5.0	0.67	3.4×10^5	0.25
6.0	0.71	3.0×10^5	0.23
12.5	0.85	1.7×10^5	0.14
25.0	0.92	9.2×10^4	0.08

Note that the fluid particle velocity at the edge is $2U_e$

2.3 Numerical specifications and initial conditions

The mesh used is a Cartesian grid with 381×381 points. The discretizations in the x_1 and x_2 directions are the same and are symmetrical with respect to the centre of the grid. The mesh spacing is uniform for the first thirty points close to the centre with a mesh spacing of $\Delta_0 = 2 \times 10^{-4}$ m. Then a stretching rate of 4% is applied to the 95 next grid points to include a large part of the radiated acoustic field in the computational domain. This stretching rate is small enough to keep the high accuracy of the numerical schemes [1]. The largest mesh spacing is thus $\Delta_{\max} = 41.5\,\Delta_0$. Finally, the mesh spacing remains uniform for the final 65 points. This mesh grid is sufficiently fine to enable an accurate propagation of the waves in the cases studied in this paper. A case has for instance been investigated with a mesh spacing twice as small and has demonstrated that the use of a finer grid does not modify the results. The origin of the axes is taken at the centre of the grid. The computational domain extends from $-3.7 \times 10^3 \Delta_0$ up to $3.7 \times 10^3 \Delta_0$ in both Cartesian directions. All the simulations are made with CFL $= c_\infty \Delta t/\Delta_0 = 1$, where c_∞ is the sound speed in the ambient medium and Δt is the time step.

The calculations are initialized by the Kirchhoff elliptic vortex. The expression of the initial velocity field is given in the Appendix A. Pressure and density are, respectively, initialized by the ambient pressure and density, p_∞ and ρ_∞. The notations used in what follows are also introduced in the Appendix A. The variable ω is the vorticity and the quantity ε, called ellipse parameter, is defined by the relation $\sigma = (1+\varepsilon)/(1-\varepsilon)$. Note that ε is linked to the excentricity e by the relation $e = 2\varepsilon^{1/2}/(1+\varepsilon)$. The radius r_e of the circle associated with the ellipse is then connected to the semi-axes by $a = r_e(1+\varepsilon)$ and $b = r_e(1-\varepsilon)$. The subscript 0 denotes a quantity taken at $t = 0$. For example, a_0 is the initial major semi-axis. The initial angular velocity of the vortex is Ω_0 and T_0 corresponds to the initial period of rotation. In all simulations, r_{e0} is set to $40\,\Delta_0$. This ensures an appropriate discretization of the geometry and of the dynamics of the vortex for $\sigma \leq 25$. The initial vorticity is $\omega_0 = 0.027/\Delta t$, providing an accurate time discretization. The parameters of the different vortices (aspect ratio σ, parameter ε, Reynolds number Re_Γ, Mach number M) are collected in Table 1.

The values taken by a and b are computed at each time step. They are evaluated from the contour of the vorticity with a threshold chosen arbitrarily as $\omega_{\max}/2$, where $\omega_{\max}$ is the maximum of vorticity in the vortex. The other parameters of the ellipse are then deduced.

3 Vortex with an aspect ratio close to unity ($\sigma_0 = 1.2$)

The case of an elliptic vortex with a small aspect ratio is first investigated. The initial aspect ratio is $\sigma_0 = 1.2$, which yields for the ellipse parameter $\varepsilon_0 = 0.09 \ll 1$. First, the aerodynamic behaviour is discussed and compared to the theoretical results developed for the Kirchhoff elliptic vortex. Then the acoustic radiation is shown and compared to the analytical solution (1). In this case, the analytical formulation reported in the Appendix B is expected to be valid.

3.1 Aerodynamic results

Figure 1a shows isolevels of vorticity at time $t/T_0 = 16$. No filamentation process is observed, even after 16 revolution periods. To understand this, the streamlines of the initial vortex in a rotating frame associated to its angular velocity $\Omega_{\text{th}} = \omega(1-\varepsilon^2)/4$ are displayed in Fig. 1b. The streamline pattern keeps the same structure during the whole evolution time. Melander et al. [17] pointed out that the return to axisymmetry can occur

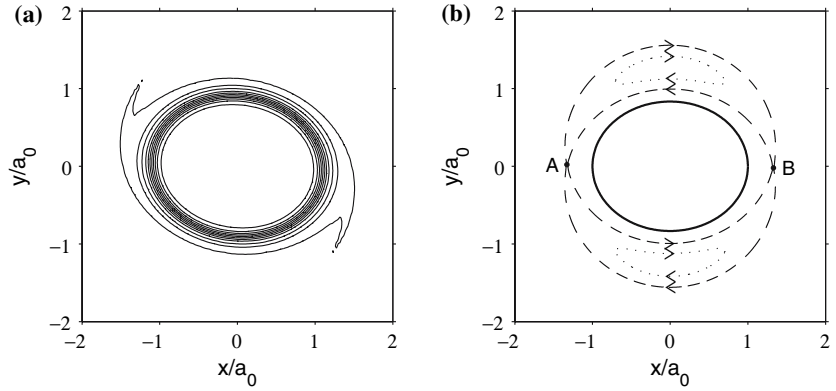

Fig. 1 Case $\sigma_0 = 1.2$. **a** Isolevels of vorticity at time $t/T_0 = 16$. Levels: 1, 5%, and from 10 to 90% of the maximum of vorticity with a 10% step. **b** Streamlines of the initial Kirchhoff vortex in a frame rotating with the angular velocity Ω_{th}. *Solid lines* edge of the vortex; *dashed lines* and *dotted lines* streamlines. The points A and B are the two saddle points

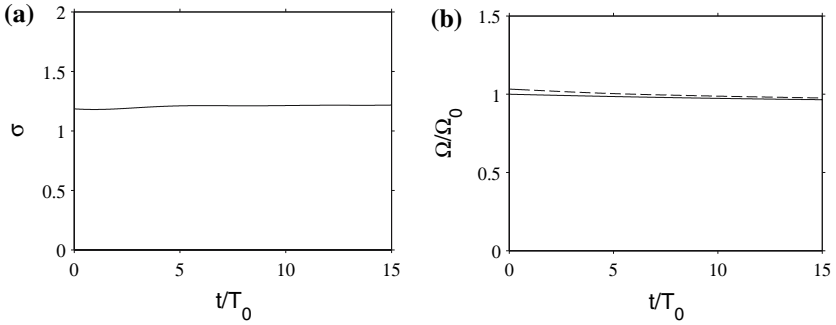

Fig. 2 Case $\sigma_0 = 1.2$. **a** Time history of σ. **b** *Solid lines* time evolution of the computed angular velocity normalized by its initial value Ω/Ω_0; *dashed lines* theoretical velocity $\Omega_{\text{th}}/\Omega_0$

only when the two saddle points A and B are located in the vorticity core. In that case, the vorticity around these points is carried away from the core and follows the streamlines, beginning the filamentation process. For a perfect top-hat vortex, the saddle points A and B are outside the patch of vorticity, as shown in Fig. 1b, and thus the shedding cannot occur. In the present computation, the viscous diffusion at the vortex edge tends to relax the gradients. However, the vortex does not become smooth enough to include the saddle points and the filamentation cannot begin. As previously observed by Dritschel [10], vortices with sufficiently steep edge gradient do not seem to return to axisymmetry. This point is also supported by the time evolution of the aspect ratio σ in Fig. 2a. The aspect ratio remains practically constant for $t < 15T_0$, indicating that the vortex rotates without significant change of form.

In Fig. 2b, the time history of the normalized computed angular velocity Ω/Ω_0 is shown to be constant and in good agreement with the theoretical value $\Omega_{\text{th}}/\Omega_0$ given by Love [16] for Kirchhoff's vortex. This theoretical velocity is calculated at each time step from the values of ε and ω, where ω is estimated by the mean integral level of vorticity inside the contour level $\omega_{\max}/2$. During the rotation, the vortex edge becomes smoother due to viscous diffusion and the area of the vortex increases slightly. This implies a low decrease of the mean integral level of vorticity and thus the small reduction of Ω_{th} observed in Fig. 2b.

3.2 Acoustic radiation

The acoustic radiation of the vortex is now investigated. The elliptic vortex radiates like a rotating quadrupole as shown with the pressure field in Fig. 3. The pressure along the line $x = y$, $x > 0$, at time $t = 16T_0$, is displayed in Fig. 4a. The magnitude of the acoustic near-field is shown to decrease rapidly when the observation point moves away from the vortex. In this figure, the computed acoustic field is compared to the analytical

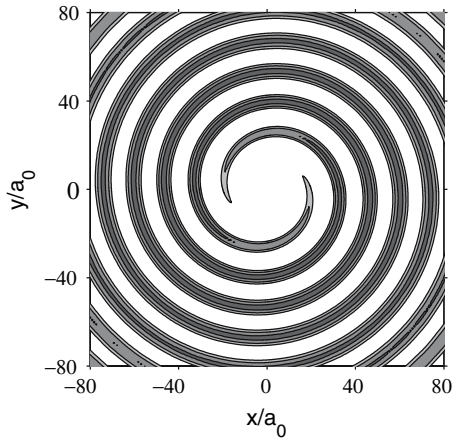

Fig. 3 Case $\sigma_0 = 1.2$. Pressure field at time $t/T_0 = 16$. Contour levels: $p_\infty - 10\,\text{Pa}$, p_∞ and $p_\infty + 10\,\text{Pa}$

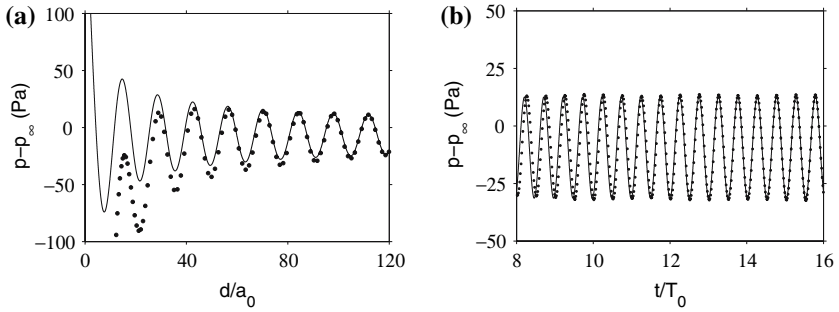

Fig. 4 Case $\sigma_0 = 1.2$. Comparison of the acoustic radiation with the analytical solution (1): *solid lines* analytical solution; *filled circle* computation. d is the distance from the vortex centre. **a** Pressure along the line $x = y$, $x > 0$ at time $t = 16T_0$. **b** Time evolution of the pressure at the point $x/a_0 = y/a_0 = 56$

formulation derived by Howe [13]:

$$p(t, r, \theta) - \overline{p}(r, \theta) \approx -\frac{\varepsilon}{8}\left(\frac{2\pi r_e}{r}\right)^{1/2} \rho_\infty U^2 M^{3/2} \cos\left(2\theta - \frac{\omega t_r}{2} + \frac{\pi}{4}\right) \tag{1}$$

where $U = r_e\omega/2$ is the maximum mean flow speed reached at the edge of the core, $M = U/c_\infty$ is the associated Mach number and $t_r = t - r/c_\infty$ is the retarded time. Details can be found in the Appendix B. This expression is appropriate for Kirchhoff's vortices with $\varepsilon \ll 1$, for which viscous effects are neglected. By considering only the first order in ε, Howe has thus obtained that the noise level is proportional to ε and that the pulsation of the radiated noise does not depend on the aspect ratio. Note that the analytical solution (1) does not provide the near-field contribution. In the present case, for $d/a_0 \geq 80$, the far acoustic field dominates the pressure field and the computational result tends to the analytical formulation, with a good agreement in frequency and level. In Fig. 4b, the comparison for an observation point in the far-field at $d/a_0 \simeq 80$ illustrates this point. The computational and the analytical solutions (1) are therefore validated in the case $\sigma_0 = 1.2$.

4 Vortex with a moderate aspect ratio ($\sigma_0 = 5$)

In this section, an elliptic vortex with a moderate aspect ratio of $\sigma_0 = 5$ is investigated. This aspect ratio corresponds to the parameter $\varepsilon_0 = 0.67$. The dynamics of the vortex should now be significantly affected by the growth of instabilities and by the return to axisymmetry. Moreover the analytical solution (1) might not be appropriate for describing the acoustic far-field.

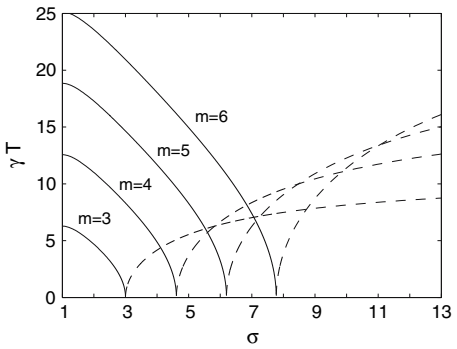

Fig. 5 Linear stability of the Kirchhoff vortex [16]. Frequency $\gamma_r T$ in *solid lines* and growth rate $\gamma_i T$ in *dashed lines* for the azimuthal modes $m = 3, 4, 5$ and 6 versus aspect ratio σ. The complex angular frequency $\gamma = \gamma_r + i\gamma_i$ is normalized by the the rotation period T of the vortex, thus $e^{\gamma_i T}$ gives the amplification of the perturbation after one rotation period

4.1 Stability of Kirchhoff's vortex

The linear stability of the Kirchhoff vortex was first studied by Love [16]. By noting δn the normal displacement of the edge of the vortex, the eigenfunction of the small perturbation in a linear analysis writes as $\delta n \sim \exp\left[i(m(\theta - \beta) - \gamma t)\right]$ where m is the azimuthal wavenumber, θ is the polar angle, β is a phase coefficient and $\gamma = \gamma_r + i\gamma_i$ is the complex angular frequency. Thus γ_i corresponds to the growth rate of the instabilities and $e^{\gamma_i T}$ gives the amplification of the disturbance after one rotation period $T = 2\pi/\Omega$. The non-dimensional angular frequency reads:

$$\gamma^2 T^2 = \pi^2 \frac{(\sigma+1)^4}{\sigma^2} \left[\left(\frac{2m\sigma}{(1+\sigma)^2} - 1 \right)^2 - \left(\frac{\sigma - 1}{\sigma + 1} \right)^{2m} \right] \tag{2}$$

The stability of the azimuthal modes $m = 3, 4, 5$ and 6 is illustrated in Fig. 5. The modes $m = 1$ and $m = 2$ are not of interest since the mode $m = 1$ is always stable and the mode $m = 2$ is neutral with $\gamma_{m=2} = 0$ for all σ. For $m \geq 3$, γ is real for small σ, which implies linear stability. Above a critical value σ_{mc}, γ becomes purely imaginary and the mode m is then linearly unstable. For the mode $m = 3$, equation (2) provides $\sigma_{3c} = 3$, and for $m > 3$, $\sigma_{mc} > \sigma_{3c}$. As a consequence, the vortex is therefore linearly stable for $\sigma < 3$, and above this value there is always at least one mode linearly unstable.

The nonlinear stability was investigated theoretically by Wan [23] and numerically by Dritschel [8], among others. Wan proved that the vortex is nonlinearly stable for $\sigma < 3$. For $3 < \sigma < 4.61$, *i.e.* when only the mode $m = 3$ is linearly unstable, only the odd perturbations are nonlinearly unstable. In a case where the initial disturbances are only even, there will be not growing instabilities. Dritschel shows indeed that even perturbations can only generate even modes through nonlinear effects and in the considered range of σ, all the even modes are stable. Finally, for $\sigma > 4.61$, at least one odd and one even mode are linearly unstable, $m = 3$ and $m = 4$ for example. Thus the vortex is nonlinearly unstable because the nonlinear effects will generate from any disturbance at least either the mode $m = 3$ or the mode $m = 4$, which are both unstable.

4.2 Aerodynamic results

The vorticity field is plotted in Fig. 6. For this case with $\sigma_0 = 5$, the filamentation process begins after about one revolution. The aspect ratio then decreases, as observed in snapshots of Fig. 6c, d. Figure 7 shows the computed streamlines leaded by the vortices in the cases $\sigma_0 = 1.2$ and $\sigma_0 = 5$. As discussed in the previous section, the saddle points are initially far from the vortex in the case $\sigma_0 = 1.2$. When σ_0 is higher, the saddle points are initially closer to the boundary of the vortex, as in the present case $\sigma_0 = 5$ in Fig. 7b, and some vorticity can reach them. Thus the filamentation process can take place.

The time history of the aspect ratio is shown in Fig. 8a. Two steps in the evolution of the vortex are visible. The first step occurs from $t = 0$ to about $t = 2T_0$. Since $\sigma_0 > \sigma_{4c}$, the vortex is initially nonlinearly unstable and the initial perturbations are growing, as observed in Fig. 6a where the vortex is no more elliptic. In the same time the shedding of vorticity begins. The vorticity field in Fig. 6a shows the first step of this process

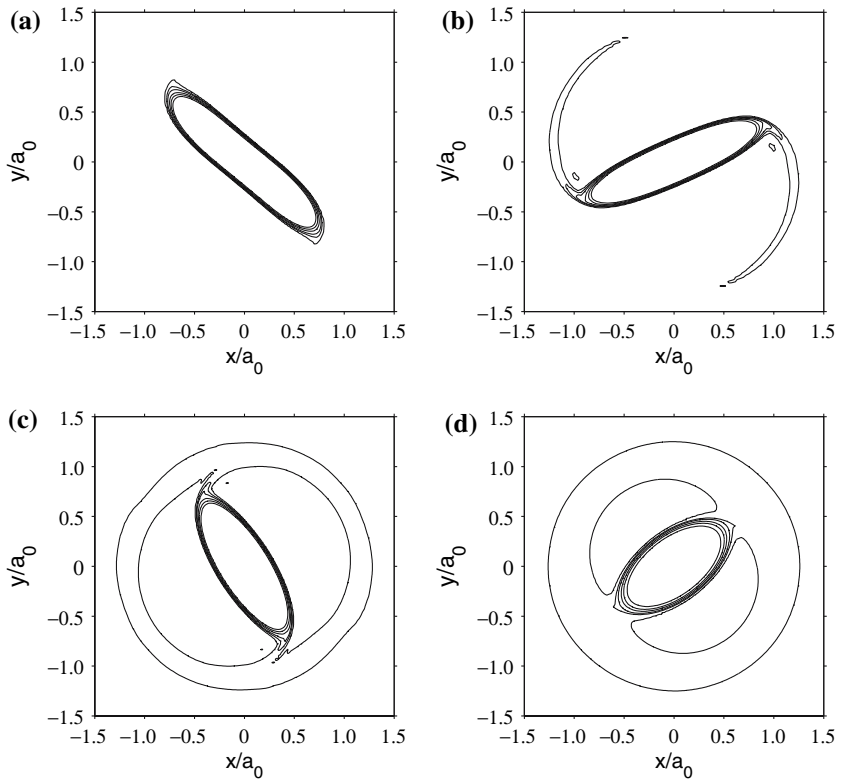

Fig. 6 Case $\sigma_0 = 5$. Isolevels of vorticity at successive times: **a** $t/T_0 = 0.91$; **b** $t/T_0 = 1.6$; **c** $t/T_0 = 4.0$; **d** $t/T_0 = 11$. Levels: 2, 10%, from 20 to 80% of the maximum of vorticity with a 20% step

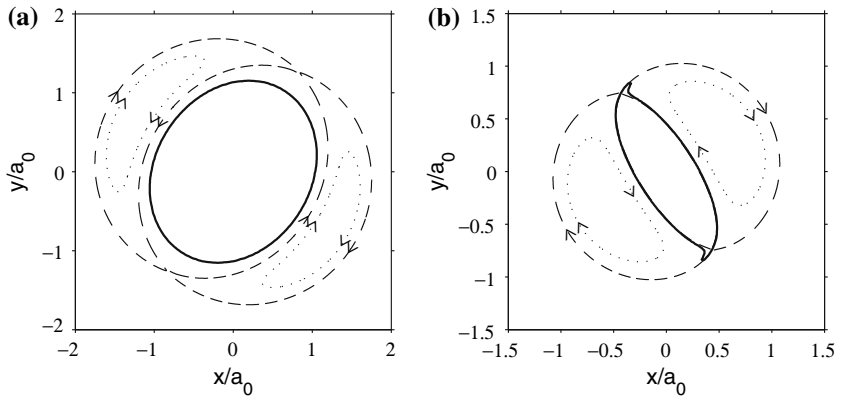

Fig. 7 Computed streamlines of the vortex in a frame rotating with the angular velocity of the vorticity patch; *solid lines* contour level of vorticity $0.1 \times \omega_{\max}$; *dashed lines* and *dotted lines* streamlines. **a** Case $\sigma_0 = 1.2$ at time $t/T_0 = 12.6$. **b** Case $\sigma_0 = 5$ at time $t/T_0 = 4.0$

and the filamentation clearly occurs in Fig. 6b. As a result, the aspect ratio decreases down to the threshold σ_{4c}. Below this value, only odd perturbations are unstable. In the present simulations, the initial aerodynamic field is even and developing perturbations are consequently even, thus the vortex becomes stable for $\sigma < \sigma_{4c}$. This first step illustrates the opposite effects of the return to axisymmetry and of the instabilities. The shedding of vorticity stabilizes the vortex whereas the growth of instabilities tends to split it. In the present case, the growth of instabilities is slow with respect to the period of rotation, therefore the return to axisymmetry is the dominant phenomenon.

From about $t = 2T_0$, the second step is observed. The vortex remains elliptic and sheds vorticity. The aspect ratio decreases and this affects the angular velocity, which increases as reported in Fig. 8b. This demonstrates

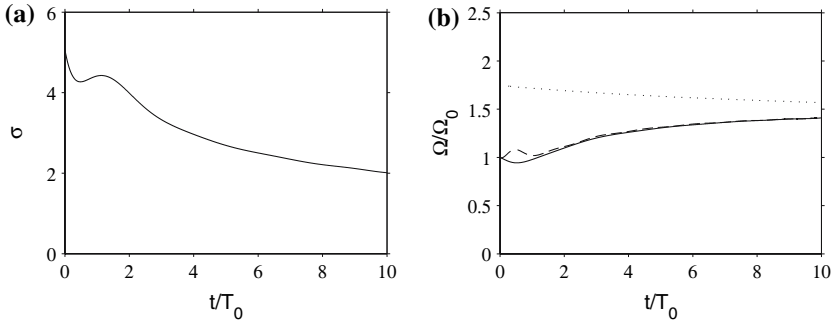

Fig. 8 Case $\sigma_0 = 5$. **a** Time evolution of σ. **b** Time history of the dimensionless angular velocity; *solid lines* effective velocity Ω/Ω_0; *dashed lines* theoretical velocity $\Omega_{\text{th}}/\Omega_0 = \omega(1-\varepsilon^2)/(4\Omega_0)$; *dotted lines* approximated velocity $\omega/(4\Omega_0)$

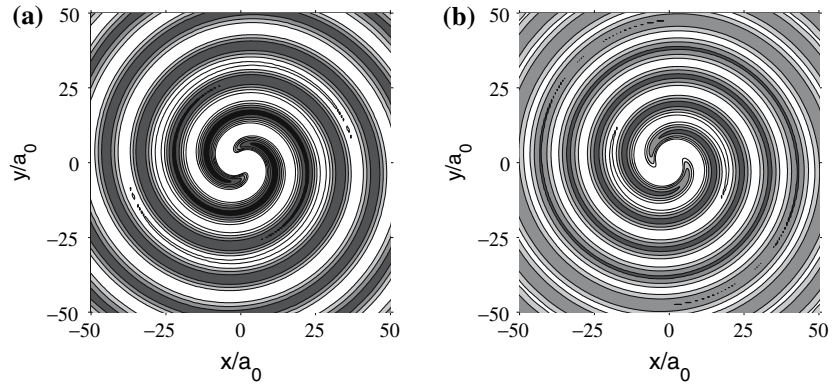

Fig. 9 Case $\sigma_0 = 5$. Pressure field at time $t/T_0 = 4.0$ (**a**) and time $t/T_0 = 11$ (**b**). Contour levels: $p_\infty - 40$ Pa, $p_\infty - 20$ Pa, p_∞, $p_\infty + 20$ Pa and $p_\infty + 40$ Pa

that the time variations of the aspect ratio now strongly modify the behaviour of the vortex. A good agreement is found between the computed velocity Ω and the theoretical velocity. Moreover, a significant discrepancy is observed between the theoretical velocity and the approximated velocity $\omega/4$, used by Howe [13] in the analytical formulation (1), showing that ε cannot be neglected if the aspect ratio is not close to unity.

The variations of the vorticity ω are directly connected to the evolution of the approximated velocity $\omega/4$, displayed in Fig. 8b. The level of vorticity inside the vortex is thus shown to decrease with time. This occurs not only because of the slight viscous dissipation but also mainly because of the shedding of vorticity. Due to the expression of the theoretical velocity of the Kirchhoff vortex $\Omega_{\text{th}} = \omega(1-\varepsilon^2)/4$, the decrease of ω implies a lowering of the angular velocity of the vortex. Thus, the filamentation tends to reduce the angular velocity through the decrease of ω. The other effect of the return to axisymmetry is the decrease of the aspect ratio and consequently of the parameter ε. The expression of the theoretical velocity Ω_{th} shows that this process implies an acceleration of the rotation. Therefore, the shedding of vorticity has two opposed effects. According to the increase of the effective velocity Ω observed in the Fig. 8b, the second effect is clearly dominant and the variations of the angular velocity are mainly due to the decrease of the aspect ratio, and not to the lowering of the vorticity level in the vortex core.

4.3 Acoustic radiation

Snapshots of the pressure field at times $t = 4T_0$ and $t = 11T_0$, and the corresponding profiles along the line $x = y$, $x > 0$ are presented in Figs. 9 and 10. The return to axisymmetry is found to affect the sound field radiated by the vortex significantly. The radiation frequency increases with time, as expected due to the increase of the angular velocity.

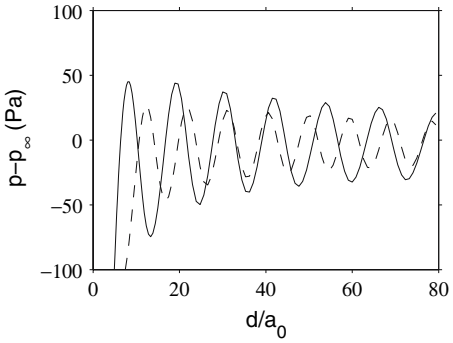

Fig. 10 Case $\sigma_0 = 5$. Pressure profiles along the line $x = y$, $x > 0$ at two different times: *solid lines* $t = 4T_0$; *dashed lines* $t = 11T_0$ (d is the distance from the vortex centre)

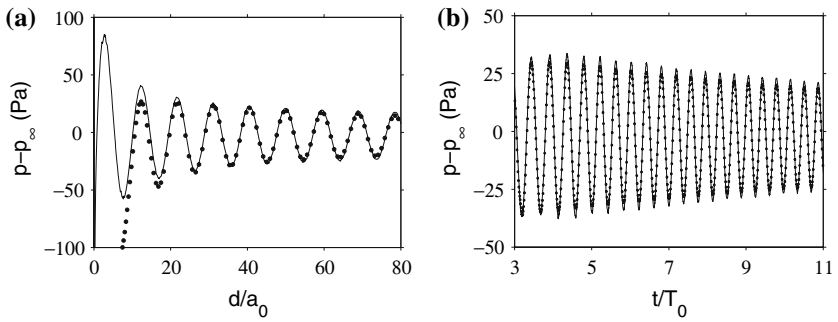

Fig. 11 Case $\sigma_0 = 5$. **a** Pressure profiles along the line $x = y$, $x > 0$ at time $t = 11T_0$; and **b** time history of the pressure at the point $x/a_0 = y/a_0 = 37$: *solid lines* analytical solution (3); *filled circle* computations (d is the distance from the vortex centre)

The classical analytical solution (1) is no more valid and, in what follows, the computed pressure field is compared to the extended formulation:

$$p(t, r, \theta) - \overline{p}(r, \theta) \approx -\frac{\varepsilon_r}{8}\left(\frac{2\pi r_{er}}{r}\right)^{1/2} \rho_\infty U_r^2 M_r^{3/2} \cos\left(2(\theta - \alpha_r) + \frac{\pi}{4}\right) \tag{3}$$

taking into account the effective motion of the vortex for the radiation frequency, see the Appendix B for details. The elliptical shape of the vortex now evolves with time, and parameters updated at the corresponding retarded times are thus used in expression (3) for computing the radiated acoustic field, namely the ellipse parameter ε and the angular position α of the vortex. The subscript r denotes the variable taken at the retarded time t_r.

Expression (3) takes into account the effective motion of the vortex and, in particular, the changes of the angular velocity in the modelling of the noise frequency, whereas in expression (1) the angular velocity is assumed to be constant. In the present case, the evolution of the radiation frequency is not negligible as shown in Fig. 10, and has indeed to be considered to provide an accurate description of the sound field.

The computed pressure profile along the line $x = y, x > 0$ at $t = 11T_0$ is plotted in Fig. 11a with the profile given by expression (3). Near the vortex, the comparison is not relevant since expression (3) does not provide the near pressure field. Farther from the vortex, a good agreement is observed between the numerical and the analytical solutions. The time history of the pressure at the location $x/a_0 = y/a_0 = 37$ is also displayed in Fig. 11b. The computed and analytical results are found to be very close. This shows that the radiation frequency is accurately predicted by expression (3) taking into account the effective rotation of the vortex. Moreover, since in expression (3) only the first order in ε is kept for the amplitude, this good agreement also indicates that the level of the radiated noise is proportional to ε. This is remarkable in the present case where the parameter $\varepsilon_0 = 0.67$ is not negligible. The present results, therefore, demonstrate that expression (3) is appropriate over a large range of aspect ratios.

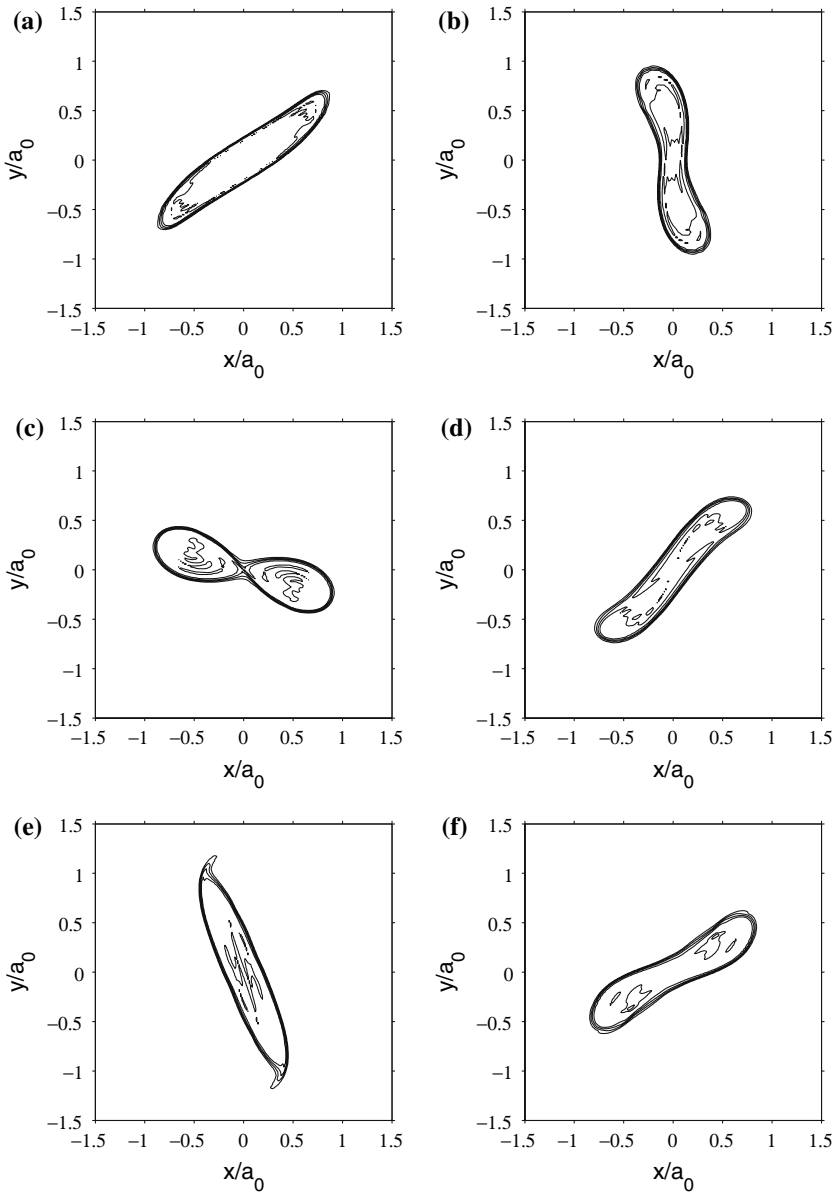

Fig. 12 Case $\sigma_0 = 6$. Isolevels of vorticity at successive times. **a** $t/T_0 = 0.096$; **b** $t/T_0 = 0.29$; **c** $t/T_0 = 0.48$; **d** $t/T_0 = 0.67$; **e** $t/T_0 = 0.87$; **f** $t/T_0 = 1.2$. Levels: 20, 40, 60 and 80% of the maximum of vorticity

5 Vortices with large aspect ratios $\sigma_0 \geq 6$

In this section, elliptic vortices with large aspect ratios $\sigma_0 \geq 6$ are investigated. For such values, the Kirchhoff elliptic vortex is linearly and nonlinearly unstable for any perturbations. In this case, the growth of instabilities is the dominant process and will cause significant deformations of the vortex. The case $\sigma_0 = 6$ is first considered. The splits of the vortex in the cases $\sigma_0 = 12.5$ and $\sigma_0 = 25$ are then computed.

5.1 Case $\sigma_0 = 6$

For the case $\sigma_0 = 6$, two stages can be distinguished in the time evolution of the vorticity field. In the first stage, an even perturbation grows and splits the ellipse into two co-rotating vortices, as shown by the vorticity snapshots in Fig. 12. The split is achieved in less than a half revolution. In this case, the growth of instabilities

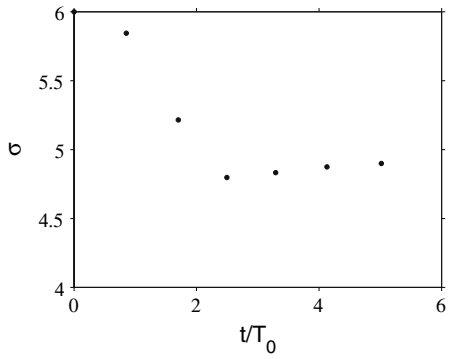

Fig. 13 Case $\sigma_0 = 6$. Time history of σ calculated when the vortex has an elliptic shape during the sequences ellipse/co-rotating vortices/ellipse

is very rapid and cannot be stopped by the return to axisymmetry. The flow configuration created by the two vortices is itself unstable. They merge to form a new elliptic vortex with an aspect ratio which remains higher than $\sigma_{4c} \approx 4.61$ as shown in Fig. 13. Therefore the new vortex is not stable, and a new switch between the two configurations, elliptic vortex and two co-rotating vortices, occurs. Several successive switches are moreover observed. The possibility of such switches has been mentioned by Dritschel [8], who showed, from energetic considerations in the inviscid case, that they may occur more easily for an aspect ratio close to six [7,8]. Note also that one sequence ellipse/co-rotating vortices/ellipse has been calculated by Vosbeek et al. [22] using the contour dynamic method. The time evolution of the aspect ratio σ at each elliptic state is shown in Fig. 13. The aspect ratio is found to decrease down to 4.8 but it remains larger than σ_{4c}. The initial decrease could be attributed to the filamentation process which is observed in Fig. 12e during the first switch. After three sequences, σ remains around 4.8.

The second stage of the vortex evolution begins at time $t \simeq 5.5T_0$. The elliptic vortex definitively splits and a stable configuration with two co-rotating vortices is obtained, as shown by the vorticity field in Fig. 14. Viscous effects then slowly relax gradients making the vortices smoother, see for instance the vorticity snapshots in Fig. 14c, d.

The time history of the pressure at the point $x/a_0 = y/a_0 = 36$ is displayed in Fig. 15. For $t < 9T_0$, the noise has been generated during the fist aerodynamic stage. Although the vorticity patch is significantly distorted during the switches, the noise seems weakly affected by the successive splits. This result suggests that it can be difficult to detect the split or the merger of vortices from acoustic measurements.

At about $t = 9T_0$, the radiation level and the frequency suddenly decrease as the final stable configuration is obtained. The sound frequency is then about half of the frequency in the first stage, and the noise level is twice as small.

5.2 Cases $\sigma_0 = 12.5$ and $\sigma_0 = 25$

Two cases of very large aspect ratios, $\sigma_0 = 12.5$ and $\sigma_0 = 25$, are finally computed. The vorticity fields of these two configurations are reported in Figs. 16 and 17 respectively. The present vortices are very unstable and thus split very early.

In the case $\sigma_0 = 12.5$, the vortex splits in less than one revolution and two co-rotating vortices are obtained. The same evolution was found by Vosbeek et al. [22] numerically using the dynamic contour method. In the case $\sigma_0 = 25$, the initial vortex is very thin and splits even earlier, in a quarter of revolution, generating four aligned vortices in Fig. 17c as described also in reference [22]. Then the two inner vortices merge and three aligned vortices are observed in Fig. 17e. Finally, one vortex remains after the merging of these three vortices. Note that in the simulations of Vosbeek et al. [22], the evolution of the four aligned vortices is quite different: the two peripheral vortices merge with their closest neighbouring vortex, forming two co-rotating vortices. The reason of this discrepancy is not clear but we can mention that Vosbeek et al. [22] used the contour dynamic method and thus do not solve the full Navier–Stokes equations.

The present results show that when the initial aspect ratio is increased, the elliptic vortex splits more rapidly and the number of created vortices is higher. Various merging can then be obtained before reaching a stable state with two co-rotating vortices or with an elliptical patch of vorticity. Note that the acoustic field is not

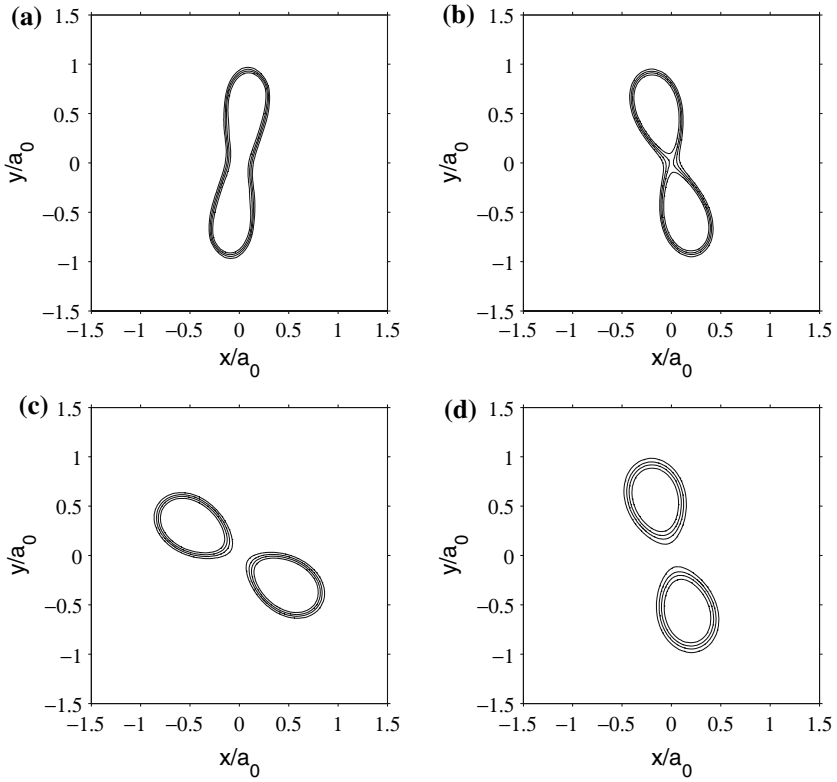

Fig. 14 Case $\sigma_0 = 6$. Isolevels of vorticity at successive times. **a** $t/T_0 = 2.9$; **b** $t/T_0 = 5.8$; **c** $t/T_0 = 8.7$; **d** $t/T_0 = 19$. Levels: 20, 40, 60 and 80% of the maximum of vorticity

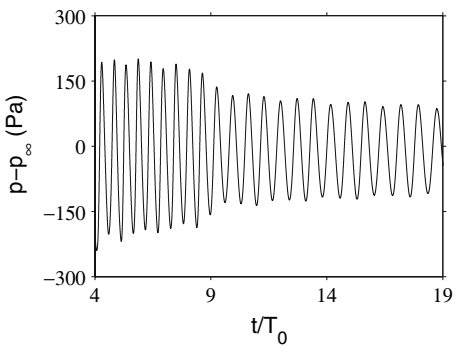

Fig. 15 Case $\sigma_0 = 6$. Time history of the pressure at the point $x/a_0 = y/a_0 = 36$

investigated in the two present cases because the aerodynamic evolutions of the vortices are too rapid to study properly the acoustic radiations.

6 Conclusions

In this paper, the aerodynamic behaviours and the acoustic radiations of elliptic vortices with different aspect ratios have been computed by solving the full 2D compressible Navier–Stokes equations. In agreement with previous numerical studies [10,17,22], the evolution of the vortex is found to be strongly dependent on the initial aspect ratio, which governs the relative weight of the return to axisymmetry and of the growth of instabilities.

For σ_0 close to unity, neither the filamentation nor the instabilities have a significant effect on the elliptic vortex. The vortex rotates with a fixed angular velocity without notable change of shape, and generates a

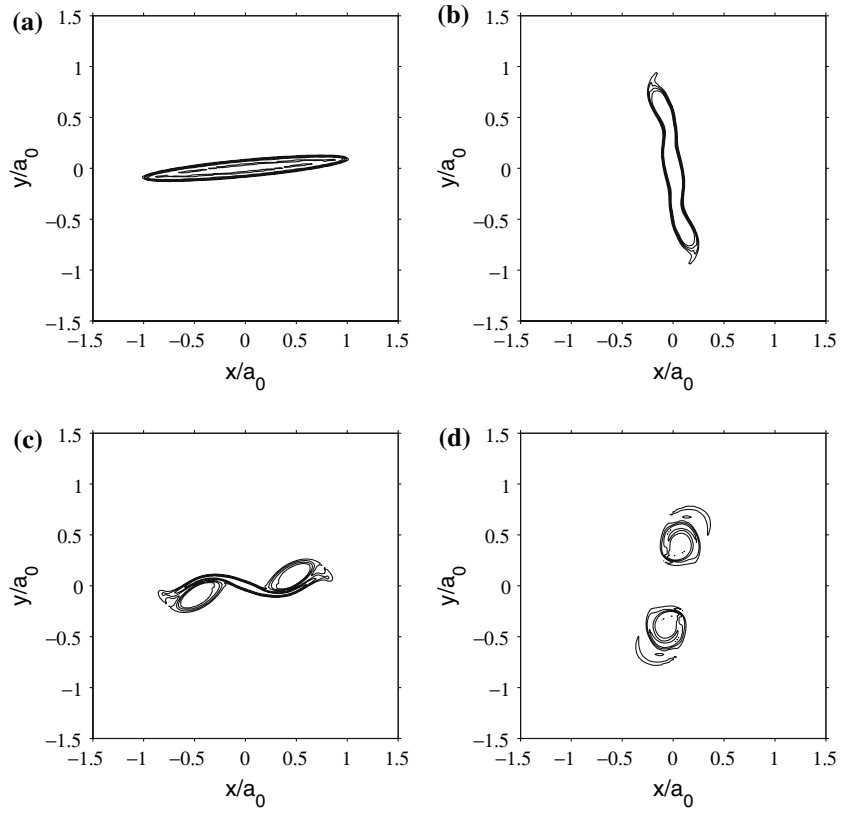

Fig. 16 Case $\sigma_0 = 12.5$. Isolevels of vorticity at successive times. **a** $t/T_0 = 0.015$; **b** $t/T_0 = 0.28$; **c** $t/T_0 = 0.54$; **d** $t/T_0 = 0.80$. Levels: 20, 40, 60 and 80% of the maximum of vorticity

constant and harmonic noise. When σ_0 is larger but remains moderate (about $2 < \sigma_0 < 6$), the return to axisymmetry is the main mechanism and stops the growth of instabilities by stabilizing the vortex. The filamentation occurs and leads to a decrease of the aspect ratio and to an increase of the angular velocity. Then the radiation frequency increases and the noise level decreases. For larger aspect ratios, the growth of instabilities dominates, and the return to axisymmetry does not occur rapidly enough to stabilize the vortex. This causes a split of the vortex in several vortices. For $\sigma_0 = 6$, switches between the elliptic state and a state with two co-rotating vortices first happen, before the vortex definitively splits. The sound field appears weakly affected by these switches. Thus the competition between the return to axisymmetry and the growth of instabilities can have notable effects on the evolution of elliptic vortices. The radiated noise then appears to be mainly affected by the decrease of the ellipse aspect ratio and not by the presence of filaments. The ellipse parameter ε is therefore the key parameter to describe the acoustic radiation of the elliptic vortex. Finally, the analytical solution developed by Howe [13] from the Lighthill's analogy for small aspect ratios has been shown to be in good agreement with the computational solution in the case $\sigma = 1.2$. For higher aspect ratios, this solution appears, however, not appropriate. An extended analytical solution for the far-field noise has been proposed, which compares well with the calculated solution in the case $\sigma_0 = 5$.

The validity of the present computational approach is clearly shown. The computations have been performed by compressible direct numerical simulation and the acoustic radiation is obtained in the same calculation. This enables one to take into account all effects, in particular compressibility and viscous diffusion. Compressible effects at moderate Mach numbers and the presence of the generated acoustic field do not seem to modify the relative balance between the return to axisymmetry and the growth of instabilities, and only one parameter, σ or ε, appears relevant to define the flow.

This work provides also reference solutions that may be useful for the development of numerical methods in aeroacoustics. The investigation of the links between the dynamics of the vortices and the acoustic field also gives basic information about of the low-frequency noise radiated by coherent vortices. Finally, the present

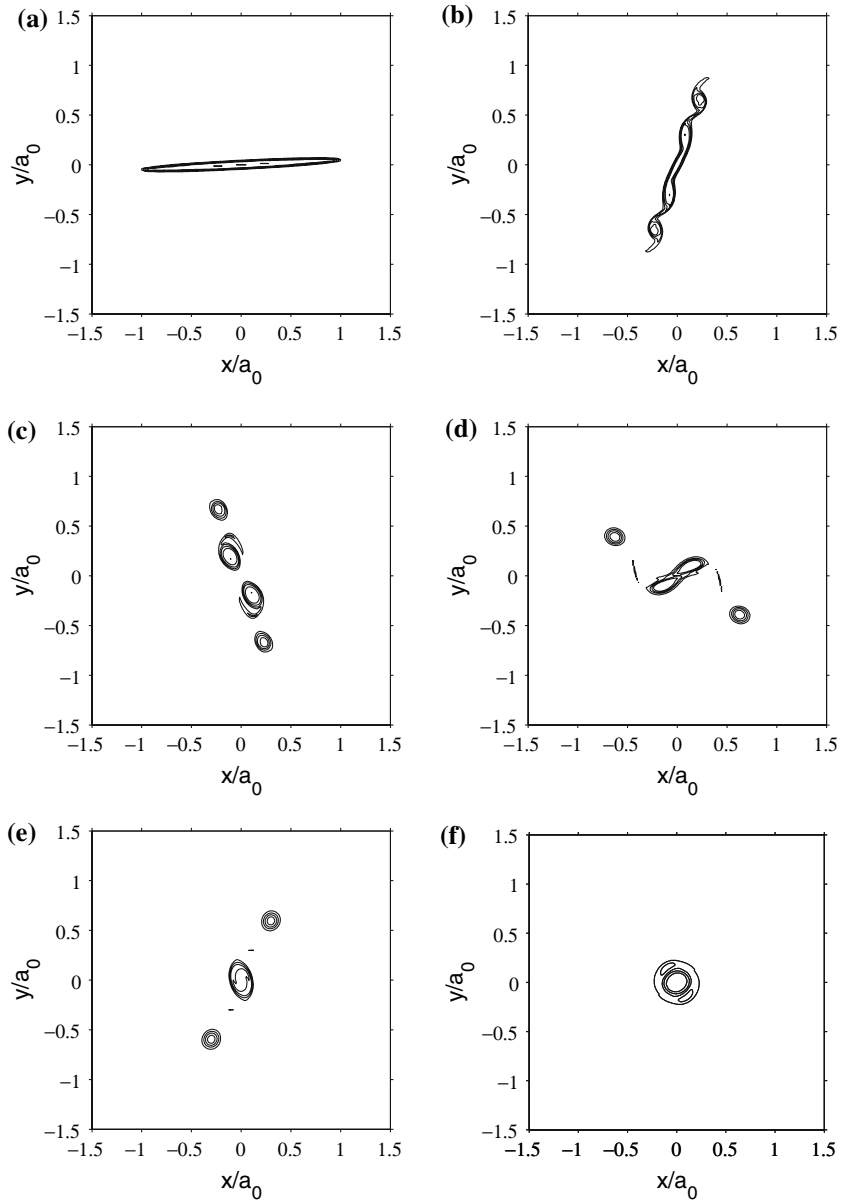

Fig. 17 Case $\sigma_0 = 25$. Isolevels of vorticity at successive times. **a** $t/T_0 = 8.1 \times 10^{-3}$; **b** $t/T_0 = 0.20$; **c** $t/T_0 = 0.32$; **d** $t/T_0 = 0.46$; **e** $t/T_0 = 0.81$; **f** $t/T_0 = 1.13$. Levels: 20, 40, 60 and 80% of the maximum of vorticity

work shows the difficulty to detect the split and the merger of vortices from the radiated pressure, as illustrated by the case $\sigma = 6$.

A Initial velocity field of the Kirchhoff vortex

An analytical expression of the initial velocity field of the elliptic vortex is required to initialize the computations. The initial vorticity distribution is an elliptic patch of uniform vorticity ω, known as the Kirchhoff vortex (1876), which is an exact analytical solution of the two-dimensional Euler equations [14,16] . There is a discontinuity of vorticity at the vortex edge located at $x_1^2/a^2 + x_2^2/b^2 = 1$, where a and b are the major and minor semi-axes of the ellipse. Two other quantities, noted r_e and ε, defined by $a = r_e(1+\varepsilon)$ and $b = r_e(1-\varepsilon)$ are used, where r_e is the radius of the circle associated with the ellipse and ε is the ellipse parameter. For $\varepsilon = 0$, the vortex is circular. The major-to-minor axes length ratio of the ellipse is denoted by $\sigma = a/b = (1+\varepsilon)/(1-\varepsilon)$.

The vortex rotates with the angular velocity $\Omega_{\text{th}} = \omega ab/(a+b)^2 = \omega(1-\varepsilon^2)/4$. The velocity field is obtained by matching a vortical field inside the vortex with a potential field outside. Within the core, the components of the velocity are, respectively in the x_1 and the x_2 directions:

$$u_1 = -\frac{a\omega}{a+b}x_2 \qquad u_2 = \frac{b\omega}{a+b}x_1$$

To obtain the velocity outside the vortex, Lamb [14] introduces the elliptic coordinates (ξ, η) defined by $x_1 = c\cosh(\xi)\cos(\eta)$ and $x_2 = c\sinh(\xi)\sin(\eta)$, where $c = (a^2 - b^2)^{1/2}$ is the focal distance. Using these coordinates, the stream function is given by:

$$\psi = \frac{1}{4}\Omega(a+b)^2\exp(-2\xi)\cos(2\eta) + \frac{1}{2}\omega ab\xi \tag{4}$$

To write the external velocity in Cartesian coordinates, the following chain-rule form can be used:

$$u_1 = -\frac{\partial\psi}{\partial x_2} = -\frac{\partial\psi}{\partial\xi}\frac{\partial\xi}{\partial x_2} - \frac{\partial\psi}{\partial\eta}\frac{\partial\eta}{\partial x_2} \qquad u_2 = \frac{\partial\psi}{\partial x_1} = \frac{\partial\psi}{\partial\xi}\frac{\partial\xi}{\partial x_1} + \frac{\partial\psi}{\partial\eta}\frac{\partial\eta}{\partial x_1}$$

The expression of the stream function (4) then yields

$$\frac{\partial\psi}{\partial\xi} = -\frac{1}{2}\Omega(a+b)^2\ \exp(-2\xi)\cos(2\eta) + \frac{\omega ab}{2}$$
$$\frac{\partial\psi}{\partial\eta} = -\frac{1}{2}\Omega(a+b)^2\ \exp(-2\xi)\sin(2\eta)$$

The different terms $\exp(-2\xi)$, $\cos(2\eta)$, $\sin(2\eta)$, $\partial\xi/\partial x_1$, $\partial\xi/\partial x_2$, $\partial\eta/\partial x_1$ and $\partial\eta/\partial x_2$ need to be expressed as functions of the coordinates x_1 and x_2. These quantities are then written as functions of $\sinh(\xi)$, $\cosh(\xi)$ and their derivatives according to x_1 and x_2. It yields:

$$\cos(2\eta) = \cos^2(\eta) - \sin^2(\eta) = \left(\frac{x_1}{c\cosh(\xi)}\right)^2 - \left(\frac{x_2}{c\sinh(\xi)}\right)^2$$

$$\sin(2\eta) = 2\sin(\eta)\cos(\eta) = \frac{2x_1x_2}{c^2\sinh(\xi)\cosh(\xi)}$$

$$\exp(-2\xi) = (\cosh(\xi) - \sinh(\xi))^2$$

The calculation of the derivatives of ξ and η is straightforward:

$$\frac{\partial\xi}{\partial x_1} = \frac{1}{\cosh(\xi)}\frac{\partial\sinh(\xi)}{\partial x_1}$$

$$\frac{\partial\xi}{\partial x_2} = \frac{1}{\sinh(\xi)}\frac{\partial\cosh(\xi)}{\partial x_2}$$

$$\frac{\partial\eta}{\partial x_1} = \frac{1}{\cos(\eta)}\frac{\partial\sin(\eta)}{\partial x_1} \tag{5}$$

$$\frac{\partial\eta}{\partial x_2} = -\frac{1}{\sin(\eta)}\frac{\partial\cos(\eta)}{\partial x_2} \tag{6}$$

Removing $\cos(\eta)$ and $\sin(\eta)$ in relations (5) and (6), the following relations are obtained:

$$\frac{\partial\eta}{\partial x_1} = -\frac{x_2}{x_1}\frac{\cosh(\xi)}{\sinh^2(\xi)}\frac{\partial\sinh(\xi)}{\partial x_1}$$

$$\frac{\partial\eta}{\partial x_2} = \frac{x_1}{x_2}\frac{\sinh(\xi)}{\cosh^2(\xi)}\frac{\partial\cosh(\xi)}{\partial x_2}$$

Finally $\sinh(\xi)$, $\cosh(\xi)$, $\partial \sinh(\xi)/\partial x_1$ and $\partial \cosh(\xi)/\partial x_2$ need to be written as functions of the primitive variables x_1 and x_2. The definition of the elliptic coordinates implies that the point (x_1, x_2) belongs to the ellipse of semi-major axis $c\cosh(\xi)$ and semi-minor axis $c\sinh(\xi)$ defined by:

$$\frac{x_1^2}{(c\cosh\xi)^2} + \frac{x_2^2}{(c\sinh\xi)^2} = 1 \tag{7}$$

By replacing $\cosh^2(\xi)$ by $1 + \sinh^2(\xi)$ or $\sinh^2(\xi)$ by $\cosh^2(\xi) - 1$ in (7), one obtains two equations, yielding

$$\begin{aligned}
\sinh(\xi) &= \frac{1}{c\sqrt{2}}\left[\lambda_- + \left(\lambda_-^2 + 4c^2x_2^2\right)^{1/2}\right]^{1/2} \\
\cosh(\xi) &= \frac{1}{c\sqrt{2}}\left[\lambda_+ + \left(\lambda_+^2 - 4c^2x_1^2\right)^{1/2}\right]^{1/2} \\
\frac{\partial \sinh(\xi)}{\partial x_1} &= \frac{1}{c\sqrt{2}}\frac{x_1}{\left[\lambda_- + \left(\lambda_-^2 + 4c^2x_2^2\right)^{1/2}\right]^{1/2}}\left[1 + \frac{\lambda_-}{\left(\lambda_-^2 + 4c^2x_2^2\right)^{1/2}}\right] \\
\frac{\partial \cosh(\xi)}{\partial x_2} &= \frac{1}{c\sqrt{2}}\frac{x_2}{\left[\lambda_+ + \left(\lambda_+^2 - 4c^2x_1^2\right)^{1/2}\right]^{1/2}}\left[1 + \frac{\lambda_+}{\left(\lambda_+^2 - 4c^2x_1^2\right)^{1/2}}\right]
\end{aligned}$$

where $\lambda_+ = x_1^2 + x_2^2 + c^2$ and $\lambda_- = x_1^2 + x_2^2 - c^2$.

All the relations needed to initialize the velocity field are now determined. Note that the expressions of $\partial\eta/\partial x_1$ and $\partial\eta/\partial x_2$ are singular in $x_1 = 0$ and in $x_2 = 0$, respectively. In these two cases, $u_2 = 0$ or $u_1 = 0$ is enforced.

B Analytical formulation of the noise radiated by the Kirchhoff vortex

In this Appendix, an analytical formulation of the far-field noise radiated by the Kirchhoff vortex is reported. The way used to derive the solution has been presented in details by Howe [13] and Dowling [6]. The viscous effects and the fluctuations of entropy are neglected. An incompressible vortical flow bounded by a volume V is considered. According to the Powell analogy, the density fluctuations outside the flow can be expressed by:

$$\rho'(t,\mathbf{x}) \approx \frac{\rho_\infty}{4\pi c_\infty^2}\frac{\partial}{\partial x_i}\int_V (\boldsymbol{\omega}\wedge\mathbf{u})_i\left(\mathbf{y}, t - \frac{|\mathbf{x}-\mathbf{y}|}{c_\infty}\right)\frac{\mathrm{d}\mathbf{y}}{|\mathbf{x}-\mathbf{y}|}$$

for a low Mach number flow, where ρ_∞ and c_∞ are respectively the mean density and the mean sound velocity in the ambient medium at rest. By considering only the far-field noise, this expression becomes:

$$\rho'(t,\mathbf{x}) \approx -\frac{\rho_\infty}{4\pi c_\infty^4|\mathbf{x}|}\frac{x_i x_j}{|\mathbf{x}|^2}\frac{\partial^2}{\partial t^2}\int_V y_j\,(\boldsymbol{\omega}\wedge\mathbf{u})_i\left(\mathbf{y}, t - \frac{|\mathbf{x}|}{c_\infty}\right)\mathrm{d}\mathbf{y} \tag{8}$$

This formulation is now applied to the Kirchhoff elliptic vortex. With the notations introduced in Appendix A, the velocity distribution within the vortex is given, in polar coordinates, by:

$$\mathbf{u} = -\frac{\omega r}{2}\left|\begin{array}{l}\sin(\theta) + \varepsilon\sin\left(\theta - \frac{1-\varepsilon^2}{2}\omega t\right) \\ -\cos(\theta) + \varepsilon\cos\left(\theta - \frac{1-\varepsilon^2}{2}\omega t\right)\end{array}\right.$$

These expressions are valid for any values of ε. In what follows, it is assumed that $\varepsilon \ll 1$, and only the first order in ε is kept. Within this restriction, the shape of the vortex in polar coordinates is $r = r_e[1 + \varepsilon\cos(2\theta - \omega t/2)]$ and the angular velocity becomes $\Omega_1 = \omega/4$. By using the method of the stationary phase and the relation $p(t,r,\theta) - \overline{p}(r,\theta) \approx c_\infty^2\rho'(t,r,\theta)$, the pressure field can be written as:

$$p(t,r,\theta) - \overline{p}(r,\theta) \approx -\frac{\varepsilon}{8}\left(\frac{2\pi r_e}{r}\right)^{1/2}\rho_\infty U^2 M^{3/2}\cos\left(2\theta - \frac{\omega t_r}{2} + \frac{\pi}{4}\right) \tag{9}$$

with $U = r_e\omega/2$, $M = U/c_\infty$ and t_r is the retarded time $t - r/c_\infty$. This expression applies only to the far-field of a Kirchhoff elliptic vortex with an aspect ratio σ close to unity. The acoustic field decreases like $r^{-1/2}$, as expected for the far-field in a two-dimensional problem. Note that the amplitude is proportional to the ellipse parameter ε, while the frequency of the noise is constant and does not depend on ε. Thus, the effect of ε on the frequency is not taken into account in this expression.

As shown in the present paper, the vortices with an initial aspect ratio not close to unity do not keep a uniform shape. The aspect ratio and the angular velocity evolve with time. In such cases, the quantities in the expression (9) have to be considered at the retarded time t_r, to take into account the propagation time between the generation and the reception of the noise. Moreover, when the aspect ratio is not close to unity, the approximated angular velocity $\Omega_1 = \omega/4$ might significantly differ from the theoretical angular velocity $\Omega_{\text{th}} = \omega(1 - \varepsilon^2)/4$ and, consequently, from the effective velocity. In this case, the expression (9) might fail in providing the radiation frequency. An extended formulation, which includes the influence of ε in both the amplitude and the frequency, can then be obtained by observing that $\omega t_r/4$ is the angular position of the vortex, α_r, at the retarded time t_r. In the case of an elliptical vortex with an aspect ratio and an angular velocity evolving with time:

$$p(t, r, \theta) - \overline{p}(r, \theta) \approx -\frac{\varepsilon_r}{8}\left(\frac{2\pi r_{er}}{r}\right)^{1/2} \rho_\infty U_r^2 M_r^{3/2} \cos\left(2(\theta - \alpha_r) + \frac{\pi}{4}\right) \tag{10}$$

where the subscript r denotes a quantity taken at the retarded time t_r. This new expression is expected to provide a better description of the radiation frequency than expression (9), because the frequency is directly linked to the effective motion of the vortex.

References

1. Bogey, C., Bailly, C.: A family of low dispersive and low dissipative explicit schemes for noise computation. J. Comput. Phys. **194**(1), 194–214 (2004)
2. Bogey, C., Bailly, C.: A family of low dispersive and low dissipative explicit schemes for noise computation. Theor. Comput. Fluid Dyn. **20**(1), 23–40 (2006)
3. Bogey, C., Bailly, C., Juvé, D.: Numerical simulation of the sound generated by vortex pairing in a mixing layer. AIAA J. **38**(12), 2210–2218 (2000)
4. Bogey, C., Bailly, C., Juvé, D.: Noise investigation of a high subsonic, moderate Reynolds number jet using a compressible LES. Theor. Comput. Fluid Dyn. **16**(4), 273–297 (2003)
5. Colonius, T., Lele, S.K., Moin, P.: Sound generation in a mixing layer. J. Fluid Mech. **330**, 375–409 (1997)
6. Crighton, D.G., Dowling, A.P., Williams, J.E.F., Heckl, M., Leppington, F.G.: Modern methods in analytical acoustics. Springer, London (1992)
7. Dritschel, D.G.: The stability and energetics of corotating uniform vortices. J. Fluid Mech. **157**, 95–134 (1985)
8. Dritschel, D.G.: The nonlinear evolution of rotating configurations of uniform vorticity. J. Fluid Mech. **172**, 157–182 (1986)
9. Dritschel, D.G.: Introduction to "contour dynamics for the euler equations in two dimensions". J. Comput. Phys. **135**, 217–219 (1997)
10. Dritschel, D.G.: On the persistence of non-axisymmetric vortices in inviscid two-dimensional flows. J. Fluid Mech. **371**, 141–155 (1998)
11. Dritschel, D.G., Legras, B.: The elliptical model of two-dimensional vortex dynamics. II: disturbance equations. Phys. Fluids **3**(5), 855–869 (1991)
12. Gloerfelt, X., Bailly, C., Juvé, D.: Direct computation of the noise radiated by a subsonic cavity flow and application of integral methods. J. Sound Vib. **266**(1), 119–146 (2003)
13. Howe, M.S.: Contributions to the theory of aerodynamic sound, with application to excess jet noise and the theory of the flute. J. Fluid Mech. **71**, 625–673 (1975)
14. Lamb, H.: Hydrodynamics (art. 159), 6th edn. Dover, New York (1932)
15. Legras, B., Dritschel, D.G.: The elliptical model of two-dimensional vortex dynamics. I: the basic state. Phys. Fluids **3**(5), 845–854 (1991)
16. Love, A.E.H.: On the stability of certain vortex motions. Proc. Lond. Math. Soc. **35**, 18–42 (1893)
17. Melander, M.V., McWilliams, J.C., Zabusky, N.J.: Axisymmetrization and vorticity-gradient intensification of an isolated two-dimensional vortex through filamentation. J. Fluid Mech. **178**, 137–159 (1987)
18. Melander, M.V., Zabusky, N.J., McWilliams, J.C.: Symmetric vortex merger in two dimensions: causes and conditions. J. Fluid Mech. **195**, 303–340 (1988)
19. Miyazaki, T., Hanazaki, H.: Baroclinic instability of kirchhoff's elliptic vortex. J. Fluid Mech. **261**, 253–271 (1994)
20. Miyazaki, T., Hirahara, K., Hanazaki, H.: The quasi-three-dimensional instability of an elliptical vortex subject to a strain field in a rotating stratified fluid. Fluid Dyn. Res. **21**, 359–380 (1997)
21. Tam, C.K.W., Webb, J.C.: Dispersion-relation-preserving finite difference schemes for computational acoustics. J. Comput. Phys. **107**, 262–281 (1993)
22. Vosbeek, P.W.C., Heijst, G.J.F. van , Mogendorff, V.P.: The strain rate in evolution of (elliptical) vortices in inviscid two-dimensional flows. Phys. Fluids **13**(12), 3699–3708 (2001)
23. Wan, Y.H.: The stability of rotating vortex patches. Commun. Math. Phys. **107**(1), 1–20 (1986)